Advances in Science and Technology Research Journal

Advances in Science and Technology Research Journal, 2025, 19(10), 422–435
https://doi.org/10.12913/22998624/208273
ISSN 2299-8624, License CC-BY 4.0

Received: 2025.06.28
Accepted: 2025.08.15
Published: 2025.09.01

Numerical analysis of the influence of the vertical position of tubes in latent heat thermal storage on the charging and discharging processes

Artur Szajding[1*], Andrzej Gołdasz[2], Kinga Korzeń[3]

[1] Faculty of Metals Engineering and Industrial Computer Science, AGH University of Krakow, al. A. Mickiewicza 30, 30-059 Krakow, Poland
[2] Faculty of Energy and Fuels, AGH University of Krakow, al. A. Mickiewicza 30, 30-059 Krakow, Poland
[3] Faculty of Non-Ferrous Metals, AGH University of Krakow, al. A. Mickiewicza 30, 30-059 Krakow, Poland
* Corresponding author's e-mail: artur.szajding@agh.edu.pl

ABSTRACT

The aim of this study is to perform a numerical analysis of the influence of the position of the tubes carrying the heat transfer fluid on the charging and discharging processes of a thermal energy storage system with a phase change material (PCM). The investigation was based on a three-dimensional numerical model of a repetitive section of the storage unit, consisting of four copper tubes and an aluminium fin acting as a heat exchanger. The model was implemented in the ANSYS Fluent environment using the built-in Solidification and Melting Model, which accounts for heat conduction, natural convection in the liquid phase, and the phase change of the PCM. Several configurations of tube placement were analysed with respect to the vertical position within the storage unit. The study evaluated their impact on the charging and discharging time, the resulting heat fluxes, temperature distribution, and the evolution of the liquid phase fraction over time. In the simulations, a PCM with a relatively high phase change temperature of approximately 78 °C was used, allowing the results to be applicable in the design of thermal storage systems integrated with conventional central heating installations. The results indicate that tube placement significantly affects the efficiency of the charging process. Lowering the tubes toward the bottom of the storage tank reduced the melting time of the PCM by 23.2%, mainly due to the enhancement of natural convection. In contrast, during the discharging process, the tube arrangement had a significantly smaller impact on the solidification time. The findings of this analysis may serve as a basis for designing more efficient stationary and mobile PCM-based thermal energy storage systems, especially in applications where compactness and fast thermal response are essential.

Keywords: phase change material, PCM, tube position optimisation, latent thermal energy storage, LHTES, charging thermal energy storage, discharging thermal energy storage, tube arrangement.

INTRODUCTION

In the face of global challenges related to reducing greenhouse gas emissions, the need to improve energy efficiency, and the growing share of renewable energy sources (RES), technologies that enable efficient storage and utilisation of thermal energy are gaining increasing importance. One of the key directions in energy technology development is the implementation of thermal energy storage (TES) systems, which balance heat supply and demand, enhance energy system reliability, and improve the energy self-sufficiency of buildings and industrial facilities [1, 2].

The use of phase change materials (PCMs) in TES is highly promising, as they enable efficient energy storage by using the latent heat of phase transitions, typically melting and solidification [3]. Compared to traditional sensible heat storage systems, PCMs offer a significantly higher energy density and facilitate temperature stabilisation during charging and discharging processes

[4]. Phase change materials have found applications in HVAC systems, solar collectors, heat pumps, heat recovery systems, and mobile energy sources [5]. One of the main challenges associated with their practical use is the inherently low thermal conductivity of most PCMs, which limits the heat transfer rate and prolongs the system response time [6].

One way to enhance the heat transfer rate in latent heat thermal energy storage (LHTES) systems is by modifying phase change materials (PCMs) to improve their thermal conductivity or to increase the amount of energy stored per unit mass. A comprehensive overview of these approaches can be found in [7].

Li et al. [8] demonstrated that carbon nanotubes can improve paraffin thermal conductivity by up to 84.6%, while Ong et al. [9] reported that surface modification of microencapsulated PCMs using multiwalled carbon nanotubes increased thermal conductivity by 87% with the addition of only 5 wt.% [10]. In [11], it was shown that the addition of 30% wt. of expanded graphite led to a 132% increase in thermal conductivity. Similarly, in [12], the addition of 5% wt. carbon fibres resulted in an 89% improvement in paraffin's thermal conductivity, while [13] recorded a 40% increase with the addition of 2% wt. carbon nanotubes.

Zhang et al. [14] prepared paraffin/graphene aerogel/copper foam composite PCMs, where the paraffin mass fraction in the composite PCM was 65% wt. and the pores density of the copper foam was 40 pores per inch. As a result, the thermal conductivity increased tenfold, from approximately 0.3 W/(m·K) to 3.0 W/(m·K).

In his study [15], Alizadeh examined the melting behaviour of a PCM enhanced with nanoparticles. The findings revealed that increasing the nanoparticle volume fraction improved thermal conductivity and reduced latent heat, resulting in a faster melting process and greater energy absorption. Based on an analysis of different volume fractions, the study identified 3% as the optimal concentration in terms of both energy storage and melting rate. However, it was also noted that exceeding this concentration could lead to nanoparticle agglomeration and sedimentation, thereby reducing the overall efficiency of the system.

Another way to overcome the low thermal conductivity of PCMs is to increase the heat exchange surface using various fins and extended surfaces [16].

Sciacovelli et al. [17] analysed the impact of Y-shaped fins with single and double branches. The use of Y-fins with double branching improved the thermal storage efficiency by 24%. Their optimisation analysis also revealed that Y-fins with smaller branch angles were more favourable for long-term operation, while fins with wider angles between branches were more effective for shorter operating periods.

Liu et al. [18] investigated the impact of two innovative fin geometries (designated as types B and C) on the PCM solidification process and compared them with conventional rectangular fins (type A). Their research showed that longitudinal fins with triangular cross sections significantly enhanced the solidification process. The best performance was obtained for type C fins, which featured a triangular cross section that decreased in size with increasing distance from the tube axis. This configuration shortened the solidification time by 38.3% compared to the standard rectangular type A fin.

In [19] the authors presented numerical simulation results for eight different configurations of triplex tube heat exchangers (TTHX), composed of three concentrically arranged tubes. The working fluid (water) flowed through the inner and outer tubes, while the space between them was filled with PCM. The simulations showed that the length of the fins had a much greater impact on the intensification of the solidification process than their thickness. The variant G was identified as the most effective configuration, achieving complete solidification of the PCM 35% faster than other configurations with the same 1mm fin thickness.

An important yet still insufficiently explored issue is the effect of the vertical positioning of heat transfer fluid (HTF) tubes within the TES chamber. The arrangement of these tubes directly influences the temperature distribution and the dynamics of natural convection, which play a crucial role in the melting process of the PCM. In studies [20] and [21] the impact of heat transfer tube configuration was investigated in TES systems, showing a significant reduction in charging time. In both cases, only the charging process was analysed, using a two-dimensional geometry with smooth tubes (without fins). A related study on sensible heat storage has shown that natural convection induced by vertical electric heating elements of different diameters can also significantly

influence temperature stratification and heating dynamics in water storage tanks [22].

This article presents an evaluation of the effect of the vertical positioning of HTF tubes on both the charging and discharging processes in a LHTES unit. The analysis was carried out based on a three-dimensional numerical model of a repetitive segment of the storage unit, consisting of four copper tubes carrying HTF and an aluminium fin serving as a heat exchanger. The model was developed in ANSYS Fluent 2023 R2. Several vertical tube placement configurations were compared by analysing the melting and solidification times, temperature distribution, evolution of the liquid phase fraction, and the resulting heat fluxes. The investigated storage system uses a PCM with a relatively high phase change temperature of approximately 78 °C. The selection of this material allows the potential application of the proposed storage unit in conventional central heating systems operating in the temperature range of 60–90 °C. The results obtained in this study may serve as a basis for designing more efficient LHTES systems, including mobile solutions, where fast charging and compact design are of key importance.

NUMERICAL MODEL

Geometry

To study how the vertical arrangement of tubes affects the charging and discharging of a latent heat thermal energy storage, a numerical analysis was carried out. A 3D model of a repeating section of the storage unit was used, which included four copper tubes and one aluminium fin. The tubes had a fixed size of $d = 12.7 \times 0.8$ mm, and the fin had dimensions of $127 \times 127 \times 1$ mm. All dimensions were given with respect to the outer diameter d of the copper tubes, as shown in Figure 1 and Table 1. The distance between neighbouring fins was 63.5 mm, and due to symmetry, the thickness of the analysed section was reduced by half to 31.75 mm. Four different vertical tube positions inside the storage unit were analysed (Table 1 and Figure 1).

Geometry A (Figure 2) had the tubes arranged in the most uniform manner, i.e., the spacing between adjacent tube axes was identical, and the distance from the heat exchanger wall was equal to half of this spacing. Geometry B (Figure 2) also had equally spaced adjacent tube axes, but the entire arrangement of tubes (upper and lower rows) was shifted downward so that the distance between the axes of the lower row and the bottom of the heat storage tank was $1d = 12.7$ mm. Geometry C (Figure 2) has the upper row of tubes positioned the same as in Geometry A (the distance between the axes of the upper row and the top of the tank is $2.5d = 31.75$ mm), while the lower row is arranged as in Geometry B. Geometry D (Figure 2) has the tubes with the greatest vertical separation ($y = 8d = 101.6$ mm), meaning that the axis of the lower row is located $1d = 12.7$ mm from the bottom of the storage tank, and the upper row is located the same distance from the top of the TES.

Properties of phase change material

The phase change material selected for the analysis was RT80HC by Rubitherm. Due to its relatively high phase change temperature (77 °C to 80 °C), it is well suited to the operating temperature range of conventional heating systems. In addition, this material is characterised by stable performance during phase change cycles, a high thermal storage capacity (220 kJ/kg), and nontoxicity [23]. Table 2 presents the physical properties of RT80HC, while Figure 3 shows the change in partial enthalpy of RT80HC as a function of temperature. In the model, the apparent specific heat was defined using piecewise linear functions based on the discrete values provided by the PCM manufacturer (Figure 3). These point values were linearly interpolated to create continuous temperature-dependent functions defined separately for melting and solidification.

Table 1. Dimensions of individual geometries

Dimensions, mm	A	B	C	D
x	$5d = 63.5$	$5d = 63.5$	$5d = 63.5$	$5d = 63.5$
y	$5d = 63.5$	$5d = 63.5$	$1.5d = 19.05$	$8d = 101.6$
y_{top}	$2.5d = 31.75$	$4d = 50.8$	$2.5d = 31.75$	$1d = 12.7$

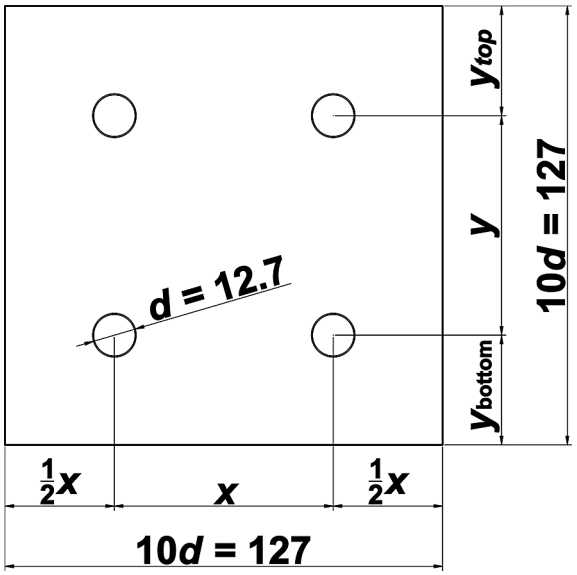

Figure 1. Characteristic dimensions of the geometry

Boundary and initial conditions

The numerical model was developed using ANSYS Fluent 2023 R2. The simulations included both the charging and discharging processes of the thermal energy storage unit.

During the charging process, a constant tube surface temperature of 95 °C was assumed, while the initial temperature of the PCM (and the fin) was set at 70°C. The charging process continued until the entire volume of the phase change material had melted. For the discharging process, the tube surface temperature was fixed at 55 °C, and the initial temperature of the PCM (and the fin) was set at 95°C. Discharging continued until the average temperature of the PCM volume reached 70 °C.

All external surfaces, including the top and bottom, were assigned adiabatic boundary conditions, while the front and rear walls were defined as symmetry boundaries. A constant temperature was applied to the surface of the heating tubes: 95 °C during charging and 55 °C during discharging of the thermal storage unit (Figure 4).

Solution methodology

In the simulations, phase change processes were modelled using the Solidification and Melting Model implemented in ANSYS Fluent. The model also accounts for laminar viscous flow and energy transfer. Natural convection was modelled by solving the full Navier–Stokes equations in the laminar regime. The buoyancy forces were accounted for by specifying the temperature-dependent density of the liquid PCM as a continuous function (calculated from the Boussinesq formula) in the material properties. The enthalpy–porosity technique was used to dampen velocities in partially solidified regions. The system's governing equations were solved using the SIMPLE algorithm. To discretise the energy and momentum equations, the Second Order Upwind scheme was applied. The pressure equation was corrected using the PRESTO scheme, as in [21, 24]. To ensure solution stability, underrelaxation factors were employed, set to 0.3 for pressure, 0.7 for velocity, 1.0 for energy, and 0.9 for the volumetric liquid fraction. The convergence criteria for the continuity, momentum, and energy equations were set to 10^{-4}, 10^{-4}, and 10^{-6}, respectively.

Mesh independence test

For geometry A, four numerical meshes were generated to perform a mesh independence test. The test was carried out for the charging process

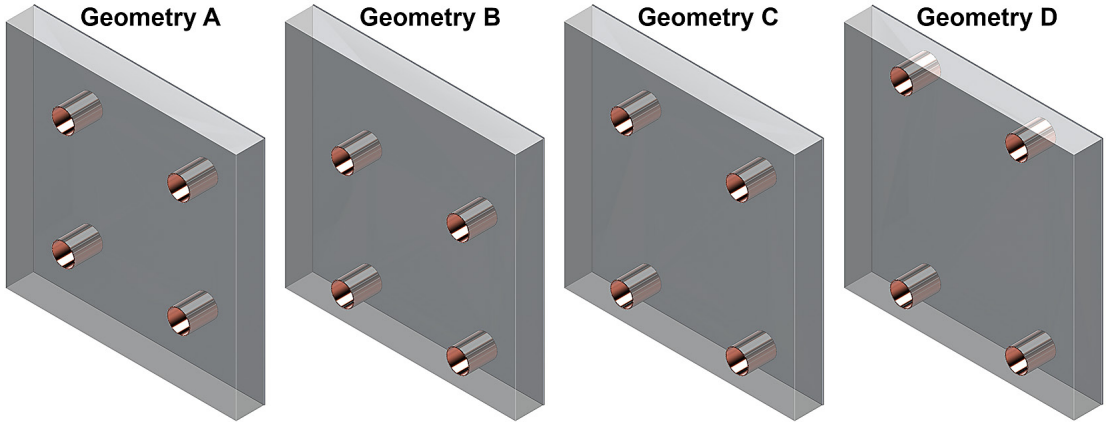

Figure 2. Investigated geometries

Table 2. Physical properties of RT80HC [23]

Melting area	77 °C ÷ 80 °C
Congealing area	80 °C ÷ 77 °C
Heat storage capacity in a temperature range 70 °C to 85 °C	220 kJ/(kg K)
Solid density	900 kg/m^3
Liquid density	800 kg/m^3
Specific heat	2 kJ/(kg K)
Thermal conductivity	0.2 W/(m K)

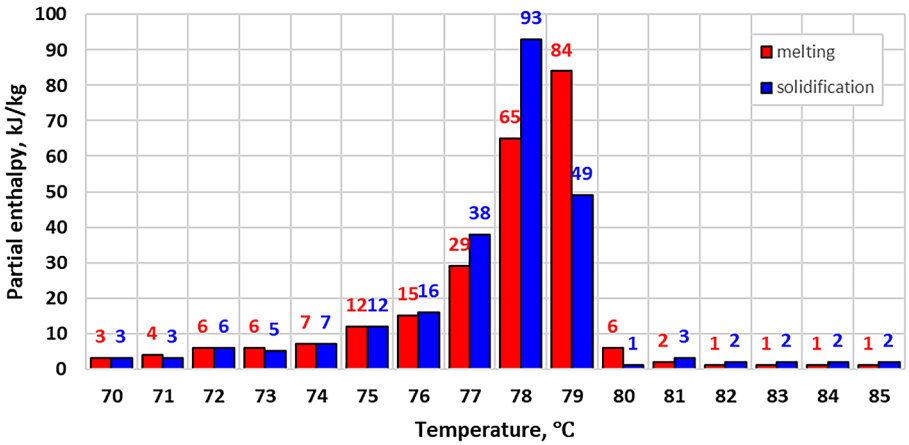

Figure 3. Change of RT80HC partial enthalpy as a function of temperature [23]

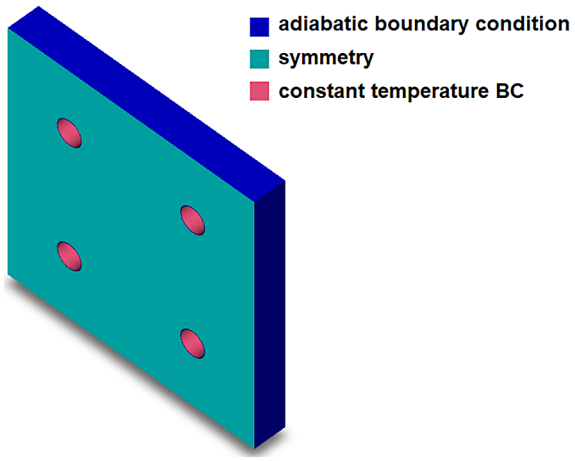

Figure 4. Boundary conditions

of the thermal energy storage unit. Table 3 presents the parameters of the generated numerical meshes. All meshes had minimum orthogonal quality values and maximum skewness values of approximately 0.5, indicating very good mesh quality. The numerical meshes were generated using polyhedral cells, and a wall-adjacent layer was applied on the boundaries of the fluid domain.

Figure 5 illustrates the influence of different mesh sizes on the liquid phase fraction of the PCM and the relative error of the liquid phase fraction. The maximum error in determining the liquid phase fraction for M3 mesh was 5.88%, with an average error of 1.97%.

The error in determining the average PCM temperature during the melting process was also evaluated. The temperature errors were lower than those in the liquid phase fraction. For mesh M3, the maximum error in determining the average temperature was 1.2%, while the average error was 0.37%.

Based on the mesh sensitivity analysis, the mesh M3 with 253 799 cells was selected for further simulations.

Model validation

The accuracy of the numerical model applied in this study has been thoroughly verified and discussed in detail in a previous work [21]. In that article, a comparative analysis was carried out between the numerical results and the experimental data obtained by Jesumathy et al. [25], who investigated a double-tube heat exchanger with paraffin wax as the PCM in the annular space and hot water flowing through the inner tube. The

Table 3. Numerical mesh

Mesh	Number of cells	Min. orthogonal quality	Ave. orthogonal quality	Max. skewness	Ave. skewness
M1	120 813	0.4849	0.8933	0.5151	0.1067
M2	181 432	0.5000	0.9006	0.5000	0.0994
M3	253 799	0.5000	0.9213	0.5000	0.0787
M4	344 059	0.5000	0.9201	0.5000	0.0799

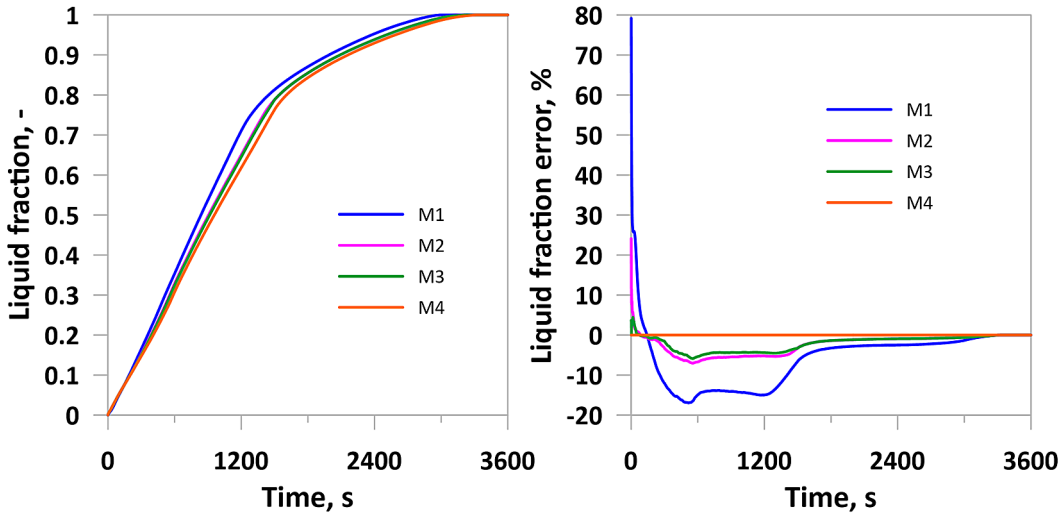

Figure 5. Effect of the numerical mesh on: a) the liquid phase fraction; b) the relative error of the liquid phase fraction

comparison, based on temperature measurements at selected locations in the PCM domain, demonstrated good agreement between the simulated and experimental results, confirming the reliability of the adopted modelling approach.

RESULTS AND DISCUSSION

Charging of the thermal storage unit

Figure 6 shows the distribution of the liquid phase fraction of the PCM during the charging process for the analysed storage geometries, at selected times: 600 s, 1200 s, 1800 s, and 2400 s. The legend is shown at the bottom of the figure. For each time step, the liquid phase fraction and the average temperature within the PCM volume are also given.

At 600 s, all configurations show the initial formation of molten regions around the heated tubes and the aluminium fin (rear surface). At the solid–liquid interface, isotherms appear concentrically around the heating tubes and parallel to the fin surface, indicating that heat conduction is the dominant mechanism. The onset of natural convection is visible in the liquid phase region. Similar observations in the initial stage of melting were made by Vikas et al. [26] for paraffin wax.

At 1200 s, the molten PCM region has significantly expanded due to intensified natural convection. Geometry B (with both rows of tubes lowered) shows the highest liquid fraction, f = 0.685, while geometry D (with lowered tubes in the bottom row and raised ones in the top row) shows the lowest, f = 0.545. This is caused by limited convective circulation in Geometry D, resulting from the relatively high position of the top tubes.

At 1800 s, the melting front progresses towards the lower part of the PCM container. Geometry B again exhibits the highest liquid fraction (f = 0.941), and Geometry D the lowest (f = 0.846). A similar value is observed for Geometry A (f = 0.855). The average temperature in the PCM is highest in Geometry B (t_{ave} = 89.3 °C) and lowest in Geometry D (t_{ave} = 84.5 °C). Despite the similar liquid fraction in geometries A and D, geometry A has a higher average temperature (t_{ave} = 88.7 °C), and a more distinct phase boundary.

At 2400 s, almost complete melting of the PCM occurs in Geometry B ($f = 0.999$), with the highest average temperature reached ($t_{ave} = 93.3$ °C). The lowest liquid fraction is observed in Geometry A ($f = 0.938$), with unmelted PCM remaining in the bottom part of the container.

Figure 7 shows the distribution of the PCM temperature during the charging process for the analysed storage geometries, at 2400 s. In all geometries, the isotherms are arranged horizontally. Higher temperatures are observed in the upper part of the TES, while lower temperatures appear in the lower part, which confirms that heat transfer occurs mainly through natural convection rather than conduction. Moreover, the highest temperatures are observed near of the heating tubes. At 2400 s, this is visible only near the tubes in the lower row. In geometries C and D, characteristic convection plumes can also be seen above the tubes in the lower row.

Although the liquid phase fraction is already high in all geometries at 2400 s (Figure 6), the temperature fields for the individual configurations still show clear differences. At this stage, the most uniform PCM temperature is found in geometry B, where both rows of tubes are lowered. In geometries C and D, temperature stratification reaches approximately halfway up the TES, indicating that the upper row of tubes did not effectively transfer heat during the entire PCM melting process. The most pronounced temperature stratification occurs in geometry A (with the lower row of tubes placed highest among all geometries) below the lower row of tubes. However, above the lower row, the PCM temperature is high and uniform, indicating that the tube spacing of 5*d* used in this configuration is appropriate. A similar effect is observed in geometry B.

Figure 8 shows the liquid phase fraction during the melting process of the PCM in the thermal storage unit for four different tube layout configurations (geometries A, B, C, and D). The dotted lines indicate the time at which full melting of the PCM (liquid phase fraction = 1) is achieved for each geometry.

At the beginning of the process, up to around 400 seconds, all geometries display a very similar melting trend, indicating that heat conduction dominates in the early stage of TES charging. After this period, an acceleration in the melting process is observed in geometries A, B, and C, while in geometry D, the melting rate remains relatively unchanged. This is due to the higher position of the top row of tubes in geometry D, which limits the development of natural convection and thus hinders the intensification of heat transfer. In the other geometries, the top row is placed lower, which promotes more effective convective heat exchange.

After approximately 800 s, geometry B shows the highest melting rate, which is associated with the lowest position of the top tubes, facilitating stronger natural convection. Around 1500 s, a noticeable slowdown is observed in geometry A, which is related to the position of the bottom row of tubes. At this stage, the PCM above the lower tubes has already melted (Figure 6) and further melting occurs mainly through heat conduction.

For the charging process of the LHTES, the tubes arrangement in geometry B (with both the upper and lower rows lowered) proves to be the most efficient. The full melting time for geometry B is 2477 s, while for geometry A (with equal spacing from all TES walls) it is 3224 s. This means that geometry B shortens the charging time by 23.2% compared to geometry A.

Figure 9 shows the change of the instantaneous heat flux (HF) during the charging process of the TES unit for four different tube arrangement configurations: A, B, C, and D. The dashed lines represent the average heat flux values for each configuration over the entire charging period.

At the beginning of the process, all geometries exhibit very high instantaneous HF values, exceeding 300 kW/(m³ PCM), due to the initially large temperature gradient between the tube surfaces and the PCM. Shortly after, the HF values drop rapidly and reach a local minimum of about 120 kW/(m³ PCM). Next, in configuration D (with the upper row of tubes located the highest), the HF decreases gradually. In configurations A–C, a secondary increase in HF is observed, indicating that the lower position of the upper row of tubes enhances heat transfer due to intensified natural convection. This effect persists the longest in geometry B, which has the upper row of tubes located the lowest. This trend is also clearly shown in Figure 6, especially around 600 s. As the charging continues, a gradual decline in HF is observed, resulting from the decreasing temperature difference and the ongoing melting of the PCM, which reduces heat transfer efficiency. In configuration B, the heat flux remains at the highest level for most of the charging period, confirming the favourable effect of tube placement on the intensification of heat transfer.

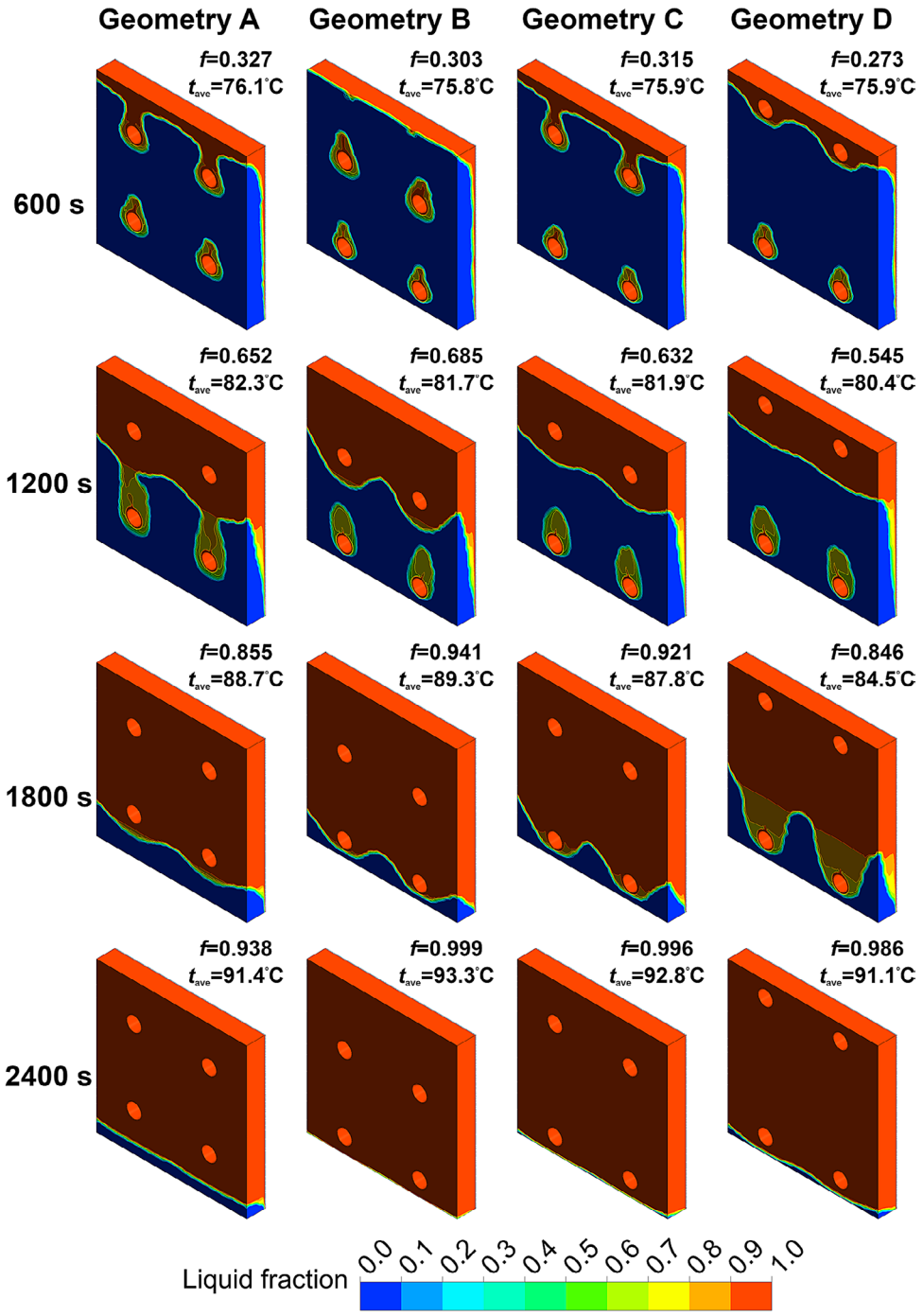

Figure 6. Distribution of the liquid phase during the charging of heat storage units (geometries A, B, C, and D)

To improve clarity, Figure 10 presents the average heat flux for the different LHTES geometries during the charging process in the form of a bar chart. The highest average heat flux was observed for geometry B – 90.05 kW/(m³ PCM), followed by geometry C – 86.63 kW/(m³ PCM), geometry D – 81.89 kW/(m³ PCM), and geometry A – 69.11 kW/(m³ PCM). This indicates that the configuration with lowered tubes in both the upper and lower rows (geometry B) allows for approximately 30.3% higher average heat flux compared to geometry A.

Figure 11 shows the stored energy per unit volume of PCM for the different thermal storage geometries. The highest value of stored energy was obtained for geometry B (57.18 kWh/(m³ PCM)). Slightly lower values were recorded for geometries A and C, while the lowest was observed for geometry D – 56.88 kWh/(m³ PCM). The differences between the geometries are very

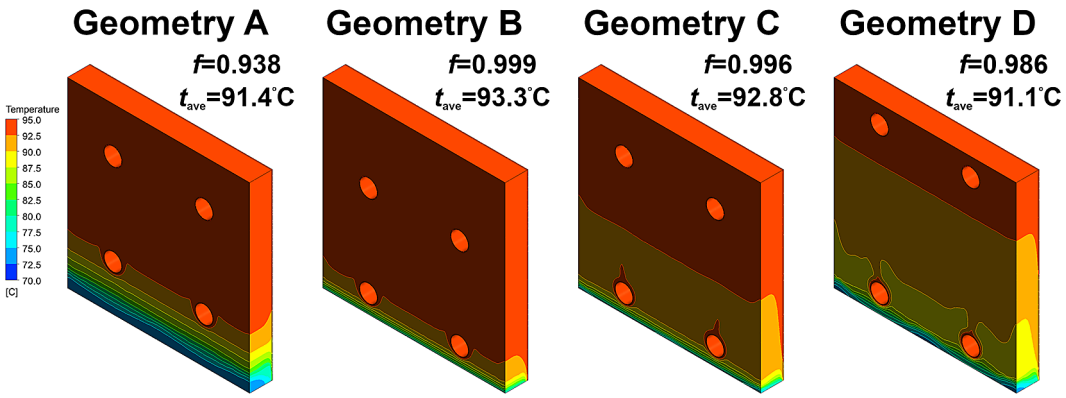

Figure 7. Temperature distribution of the PCM during the charging process in heat storage units with geometries A, B, C, and D

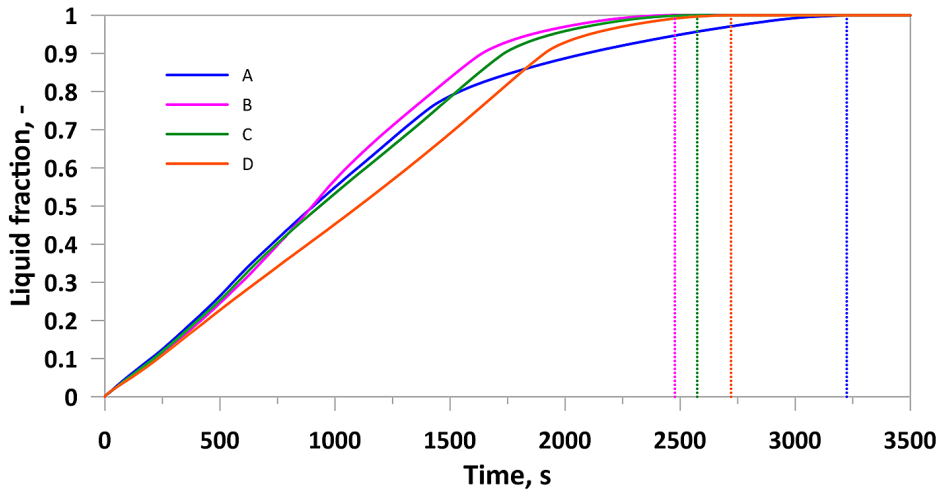

Figure 8. Liquid fraction of PCM during the TES charging process for different geometries

small (below 1%), which indicates that the total energy storage capacity does not significantly depend on the tube arrangement, but rather on the total PCM volume and the boundary conditions of the process.

Discharging of the thermal storage unit

Figure 12 presents the distribution of the liquid phase fraction of the PCM during the discharging (solidification) process in the analysed thermal storage geometries for selected time intervals: 600 s, 1200 s, 1800 s and 2400 s.

At 600 s all geometries still show relatively large volumes of the liquid phase. The solid phase is mainly concentrated around the cooling tubes and parallel to the surface of the fin, indicating heat conduction. The phase distribution follows a layered pattern, with the upper part of the tank containing the most liquefied material.

In the following time steps, the solidification process progresses similarly across all configurations and the obtained values of the liquid phase fraction and average PCM temperature differ only slightly.

After 2400 s the lowest liquid phase fraction ($f = 0.105$) and the lowest average PCM temperature (t_{ave} = 70.2 °C) were obtained for geometry A. In contrast, geometry B shows the highest liquid phase fraction ($f = 0.135$), and geometry D the highest average temperature (t_{ave} = 71.1 °C).

Although the differences are small, they confirm that heat transfer during solidification is mainly governed by conduction. The most solidified material is concentrically distributed around the tubes, perpendicular to the fin, and in the lower part of the thermal storage unit.

It can be concluded that the arrangement of the tubes in the thermal storage does not significantly affect the discharging efficiency, and the

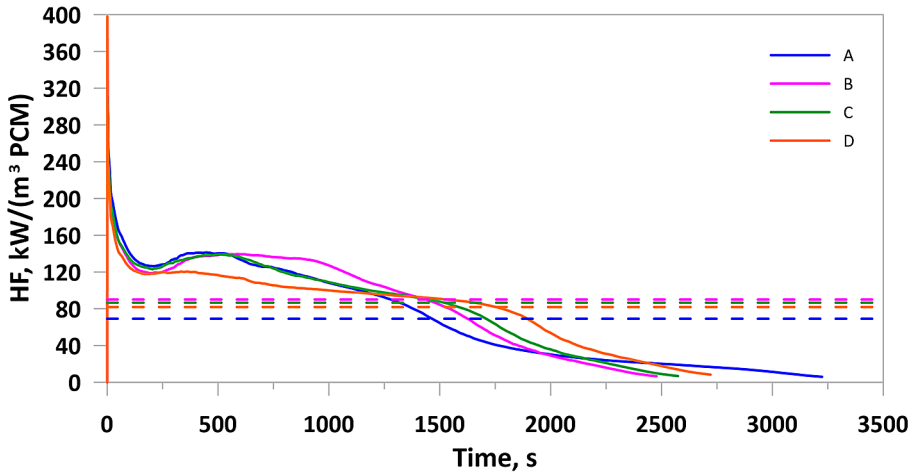

Figure 9. Heat flux for various LHTES geometries during the charging process

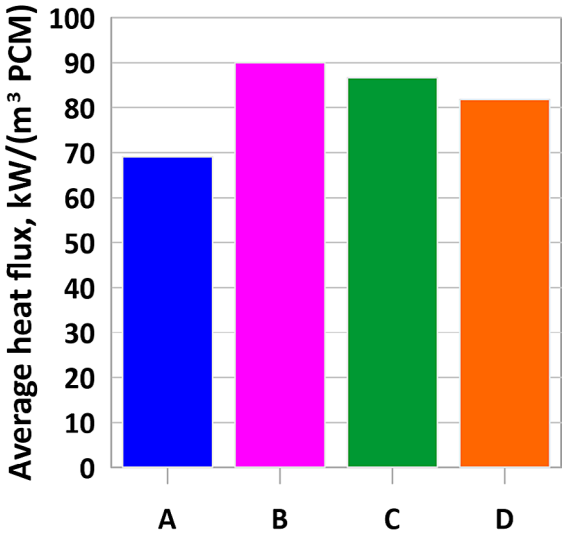

Figure 10. Average heat flux for various LHTES geometries during the charging process

most favourable solidification behaviour was observed for the geometry with evenly spaced tubes (geometry A)

Figure 13 shows the temperature distribution in the PCM after 2400 s of the discharging process for the four analysed geometries (A–D). Lower PCM temperatures are concentrated near the tubes and fins as well as in the lower part of the TES domain. In all configurations, concentric zones with densely packed isotherms are observed around the tubes, indicating intense cooling by conduction. Configuration A (with evenly distributed tubes) exhibits the lowest liquid phase fraction and the lowest average PCM temperature. This results from the uniform arrangement of the tubes in the TES, where the concentric isotherms around the tubes enable unobstructed heat transfer by conduction. In the case of the other geometries, the concentric shape of the isotherms is distorted by the proximity of the lower row of tubes to the bottom of the heat storage, which limits heat conduction.

Figure 14 shows the liquid fraction of the PCM during the TES discharging process for geometries A, B, C and D. The dashed lines indicate the moment of complete LHTES discharging, defined as the point at which the average temperature within the PCM volume decreases to 70 °C.

The trends for all geometries are very similar, indicating the dominant role of heat conduction in the PCM solidification process. Geometry A (with equal spacing between the tubes and all TES walls) shows a slightly faster decrease in

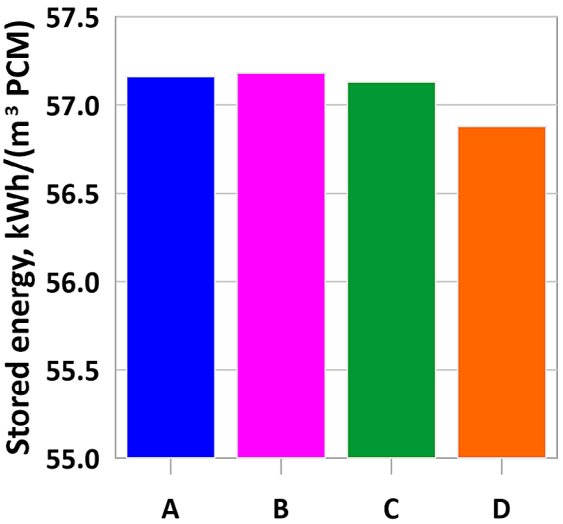

Figure 11. Stored energy for different LHTES geometries

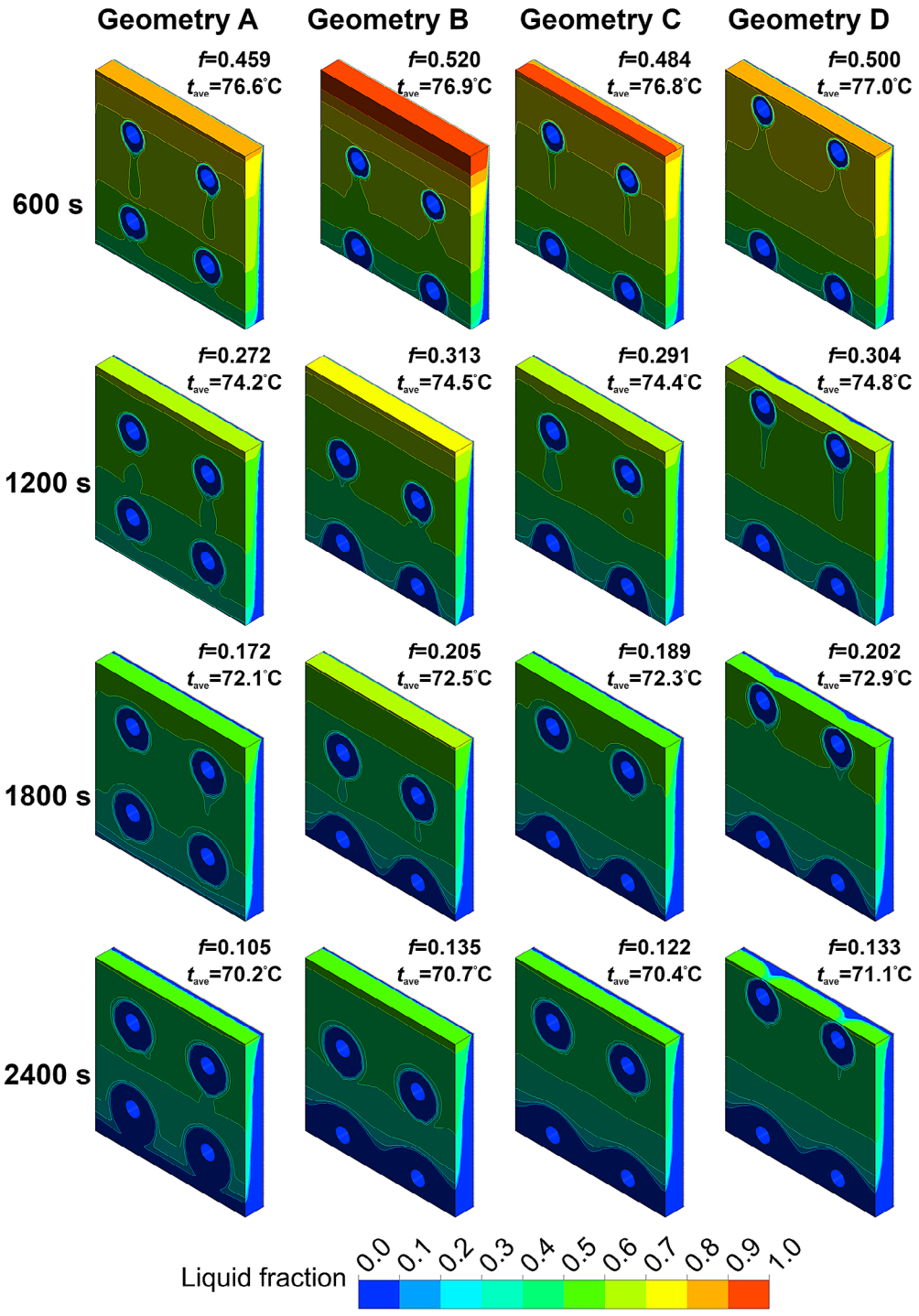

Figure 12. Distribution of the liquid phase during the discharging of heat storage units (geometries A, B, C, and D)

the liquid phase fraction compared to the other configurations. The shortest discharging time was obtained for geometry A (2474 s), followed by geometry C (with lower positioned bottom tubes compared to geometry A) – 2538 s (i.e. 2.5% longer than A), geometry B – 2603 s (approximately 5% longer than A), and geometry D – 2772 s (10.8% longer than A).

These differences suggest that the tube arrangement within the TES also affects the heat transfer efficiency during the discharging process, although this effect is less pronounced than during charging. A uniform tube distribution in the thermal storage unit (that is, equal spacing between tubes and half that spacing between the tubes and TES walls) helps to shorten the discharging time.

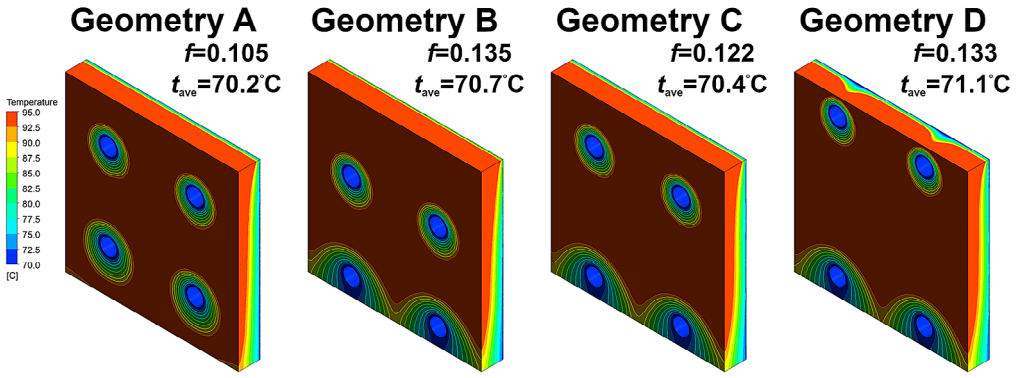

Figure 13. Temperature distribution of the PCM during the discharging process in heat storage units with geometries A, B, C, and D

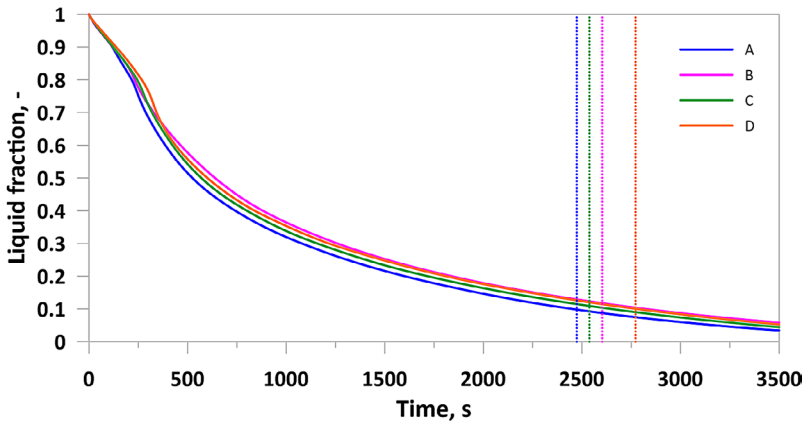

Figure 14. Liquid fraction of PCM during the TES discharging process for different geometries

Figure 15 presents the average heat flux for various LHTES geometries during the discharging process. The highest value was obtained for geometry A – 72.48 kW/(m³ PCM), while the lowest was for geometry D – 64.2 kW/(m³ PCM), which is approximately 11.4% lower than for geometry A. Geometry B, which performed best during the charging process, achieved 67.72 kW/(m³ PCM) during discharging, which is about 7.5% lower than geometry A.

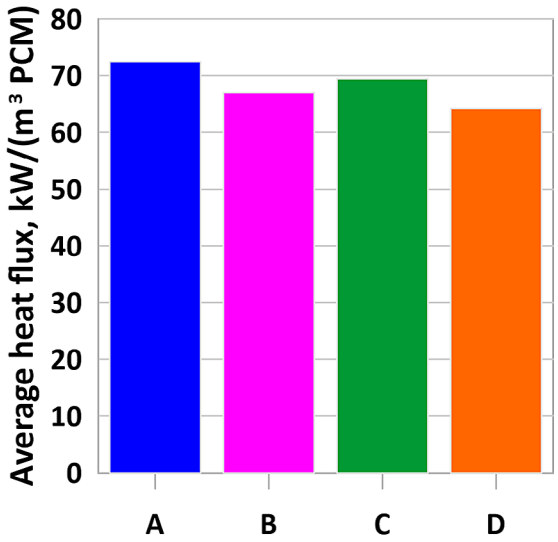

Figure 15. Average heat flux for various LHTES geometries during the discharging process

This confirms that a uniform tube distribution within the PCM volume supports more efficient heat transfer during the discharging process. However, the impact of tube arrangement is more significant during TES charging than during discharging.

CONCLUSIONS

This paper presents an analysis of the impact of the vertical arrangement of heat exchanger tubes on the charging and discharging processes of a thermal energy storage system containing phase change material. Four different geometric configurations (A–D) were investigated in terms of liquid phase distribution, heat flux density, and stored energy.

During the charging process, conduction was the dominant heat transfer mechanism at the beginning, followed by natural convection. Geometry B, featuring lowered tubes in both the upper and lower rows, demonstrated the highest efficiency: the fastest melting progression, the highest instantaneous and average heat flux densities, and the shortest full charging time for the TES (23.2% shorter than for geometry A). The total stored energy was similar across all variants (differences below 1%).

During discharging, the differences between geometries were smaller, with conduction being the prevailing mechanism. Geometry A (with uniformly spaced tubes) provided the shortest discharging time and the highest average heat flux density. The difference in discharging time between geometries A and B (which had the shortest charging time) was only 5%.

Based on the analysis of the obtained results, the following conclusions were drawn:

- The arrangement of the tubes significantly influences the efficiency of the charging process, mainly through the enhancement of natural convection.
- Geometry B, with lowered tubes in both the lower and upper rows, is the most efficient during charging and allows a significant reduction in charging time (by 23.2% compared to geometry A).
- During discharging, the effect of tube arrangement is smaller, with conduction playing the dominant role.
- The best discharging performance was achieved with geometry A, featuring a uniform tube distribution (its discharging time was 5% shorter compared to geometry B).
- A well design tube system increases heat transfer efficiency in the LHTES, especially during charging, without the need for additional material costs.
- The tube layout design process should consider the differences in the dominant heat transfer mechanisms during melting (convection) and solidification (conduction) of the PCM.
- Geometry B can be considered optimal, as it ensures by far the shortest TES charging time and a relatively short discharging time (only 5% longer than for geometry A). It therefore represents the best compromise between charging speed and discharging efficiency.

Acknowledgements

This research was partially supported by the National Centre for Research and Development, Poland, under the project "Development of a mobile heat store to utilize waste heat for the PTEP company," New Energy Technologies II (grant no. NTE-II/0004/2022), and partially supported by the Ministry of Science and Higher Education, Poland (grant no. 16.16.210.476 and grant no. 16.16.110.663, AGH University of Science and Technology).

REFERENCES

1. Dinçer İ., Rosen M.A. Thermal Energy Storage Systems and Applications, Wiley 2021.
2. Szajding, A., Kuta M., Cebo-Rudnicka A., Rywotycki M. Analysis of work of a thermal energy storage with a phase change material (PCM) charged with electric heaters from a photovoltaic installation. International Communications in Heat and Mass Transfer 2023, 140, 106547. https://doi.org/10.1016/j.icheatmasstransfer.2022.106547
3. Sharma A., Tyagi V.V., Chen C.R., Buddhi D. Review on thermal energy storage with phase change materials and applications. Renewable and Sustainable Energy Reviews 2009, 13(2), 318–345. https://doi.org/10.1016/j.rser.2007.10.005
4. Boldoo T., Chinnasamy V., Cho H. Enhancing efficiency and sustainability: Utilizing high energy density paraffin-based various PCM emulsions for low-medium temperature applications. Energy 2024, 303, 131988. https://doi.org/10.1016/j.energy.2024.131988
5. Faraj K., Khaled M., Faraj J., Hachem F., Castelain C. A review on phase change materials for thermal energy storage in buildings: Heating and hybrid applications. Journal of Energy Storage 2021, 33, 101913. https://doi.org/10.1016/j.est.2020.101913
6. Benyahia I., Al-Ghamdi M. F., Abderrahmane A., Younis O., Laouedj S., Guedri K., Alahmer A. Comprehensive thermal analysis of a nano-enhanced PCM in a finned latent heat storage system. International Communications in Heat and Mass Transfer 2025, 165, Part B, 109106. https://doi.org/10.1016/j.icheatmasstransfer.2025.109106
7. Pielichowska, K., Pielichowski, K. Phase change materials for thermal energy storage. Progress in Materials Science 2014, 65, 67–123. https://doi.org/10.1016/j.pmatsci.2014.03.005
8. Li M., Guo Q., Su Y. The thermal conductivity improvements of phase change materials using modified carbon nanotubes. Diamond and Related Materials 2022, 125, 109023. https://doi.org/10.1016/j.diamond.2022.109023

9. Ong P. J., Png Z. M., Debbie Soo X. Y., Wang X., Suwardi A., Chua M. H., Xu J., Zhu Q. Surface modification of microencapsulated phase change materials with nanostructures for enhancement of their thermal conductivity. Materials Chemistry and Physics 2022, 277, 125438. https://doi.org/10.1016/j.matchemphys.2021.125438
10. Xu C., Zhang H., Fang G. Review on thermal conductivity improvement of phase change materials with enhanced additives for thermal energy storage. Journal of Energy Storage 2022, 51, 104568. https://doi.org/10.1016/j.est.2022.104568
11. Wang T., Yang T., Kao C., Yan W., Ghalambaz M. Paraffin core-polymer shell micro-encapsulated phase change materials and expanded graphite particles as an enhanced energy storage medium in heat exchangers. Advanced Powder Technology 2020, 31(6), 2421–2429. https://doi.org/10.1016/j.apt.2020.04.006
12. Zhu X., Han L., Yang F., Jiang J., Jia X. Lightweight mesoporous carbon fibers with interconnected graphitic walls for supports of form-stable phase change materials with enhanced thermal conductivity. Solar Energy Materials and Solar Cells 2020, 208, 110361. https://doi.org/10.1016/j.solmat.2019.110361
13. Cao X., Li C., He G., Tong Y., Yang Z. Composite phase change materials of ultra-high molecular weight polyethylene/paraffin wax/carbon nanotubes with high performance and excellent shape stability for energy storage/ Journal of Energy Storage 2021, 44, Part B, 103460. https://doi.org/10.1016/j.est.2021.103460
14. Zheng X., Gao X., Huang Z., Li Z., Fang Y., Zhang Z. Form-stable paraffin/graphene aerogel/copper foam composite phase change material for solar energy conversion and storage. Solar Energy Materials and Solar Cells 2021, 226, 111083. https://doi.org/10.1016/j.solmat.2021.111083
15. Alizadeh, A. Application of nanoparticles in the process of phase change paraffin in a chamber. Advances in Science and Technology Research Journal 2019, 13(3), 113–119. https://doi.org/10.12913/22998624/110372
16. Zayed M. E., Zhao J., Li W., Elsheikh A. H., Elbanna A. M., Jing L., Geweda A.E. Recent progress in phase change materials storage containers: Geometries, design considerations and heat transfer improvement methods. Journal of Energy Storage 2020, 30, 101341. https://doi.org/10.1016/j.est.2020.101341
17. Sciacovelli A., Gagliardi F., Verda V. Maximization of performance of a PCM latent heat storage system with innovative fins. Applied Energy 2015, 137, 707–715. https://doi.org/10.1016/j.apenergy.2014.07.015
18. Liu, S., Peng, H., Hu, Z., Ling, X., Huang, J. Solidification performance of a latent heat storage unit with innovative longitudinal triangular fins. International Journal of Heat and Mass Transfer 2019, 138, 667–676. https://doi.org/10.1016/j.ijheatmasstransfer.2019.04.121
19. Al-Abidi, A. A., Mat, S., Sopian, K., Sulaiman, M. Y., Mohammad, A. T. Numerical study of PCM solidification in a triplex tube heat exchanger with internal and external fins. International Journal of Heat and Mass Transfer 2013, 61, 684–695. https://doi.org/10.1016/j.ijheatmasstransfer.2013.02.030
20. Obai Y., Laouedj S., Abdeldjalil B., Naef A. A. Qasem. Numerical analysis of the influence of inner tubes arrangement on the thermal performance of thermal energy storage unit. Energies 2023, 16(9), 3663. https://doi.org/10.3390/en16093663
21. Szajding A., Gołdasz A., Łach Ł., Eichler P. The impact of tube arrangement in latent heat thermal energy storage on the melting rate of phase change material. Advances in Science and Technology Research Journal 2024, 18(9), 366–374. https://doi.org/10.12913/22998624/194888
22. Beithou N., Abdallatif N., Khalid M. B., Attar H., Alsaqoor S., Alahmer A., Borowski G., As'ad S., Andruszkiewicz A., Al-dalain R. Enhancing thermal performance of hot storage tanks through chimney-type electric heating and natural circulation. Advances in Science and Technology Research Journal 2024, 18(3), 151–160. https://doi.org/10.12913/22998624/186160
23. Data Sheet RT80HC. www.rubitherm.eu (last access date 2025.06.12)
24. Kazemi, M., Hosseini, M. J., Ranjbar, A. A., Bahrampoury, R. Improvement of longitudinal fins configuration in latent heat storage systems. Renewable Energy 2018, 116, 447–457. https://doi.org/10.1016/j.renene.2017.10.006
25. Jesumathy, S. P., Udayakumar, M., Suresh, S., Jegadheeswaran, S. An experimental study on heat transfer characteristics of paraffin wax in horizontal double tube heat latent heat storage unit. Journal of the Taiwan Institute of Chemical Engineers 2014, 45(4), 1298–1306. https://doi.org/10.1016/j.jtice.2014.03.007
26. Vikas, Yadav A., Samir S., Arıcı M. A comprehensive study on melting enhancement by changing tube arrangement in a multi-tube latent heat thermal energy storage system. Journal of Energy Storage Volume 2022, 55, Part B, 105517. https://doi.org/10.1016/j.est.2022.105517